An RTS-Based Near-Field MIMO Measurement Solution—A Step Toward 5G

Penghui Shen, *Student Member, IEEE*, Yihong Qi, *Senior Member, IEEE*, Wei Yu, *Member, IEEE*, James L. Drewniak, *Fellow, IEEE*, Ming Yu, *Fellow, IEEE*, and Fuhai Li, *Member, IEEE*

***Abstract*— Multiple-input and multiple-output (MIMO) over-the-air (OTA) measurements have helped 4G wireless systems significantly for the communication throughput and to enhance the network stability. However, there remains a potential challenge, which may substantially obstruct the OTA test methodologies being adopted in 5G evaluations. According to the MIMO OTA measurement standards, throughput tests should be conducted in the far-field. As a result, a general system covering all the 4G frequency bands should be larger than 3.6 m, and even tens of meters for 5G. In addition to the cost of the chamber hardware, a sizeable footprint of building space is also required for the test system. Consequently, conducting far-field tests directly incurs excessively high costs in 5G. A compact system with dimensions of 1.9 m for 5G MIMO OTA is proposed in this paper, where a near-field to far-field transformation method is adopted into the current standard MIMO OTA test approach (the radiated two-stage approach), and the throughput in the near field is measured. Compared to existing test systems, the compact solution can achieve a cost reduction by at least an order of magnitude and obtain comparable results as a full-scale certification system.**

***Index Terms*— 5G, multiple-input and multiple-output (MIMO), near field to far field, radiated two-stage.**

I. Introduction

An EXPLOSIVE growth in the quantity of multiple-input and multiple-output (MIMO) wireless terminals has been seen in the last decade [1]–[4]. Over-the-air (OTA) evaluations of MIMO wireless device radio frequency (RF) performance are critical for the user experience and ensuring that the in-band and out-band interference does not significantly impact the wireless network quality and reliability [5], [6]. However, currently most of wireless products cannot be fully measured for estimating the RF performances, due to the test cost.

MIMO OTA testing is specified by international organizations such as the Cellular Telecommunication and Internet Association (CTIA) and the 3rd Generation Partnership Project (3GPP) [7], [8]. The standards specify that OTA tests should be conducted in the far-field, since in the near field, the test errors resulting from the test distance cannot be quantified and may not be negligible. The standard far-field MIMO OTA measurement system is of large dimensions (tens of meters for 5G), with a high hardware and real estate cost [9], [10]. This would limit the OTA measurement accessibility for many wireless device manufacturers. There is a need to theoretically analyze and resolve the near-field-related MIMO throughput measurement uncertainties, so that the 5G measurement test range can be reduced. A compact size MIMO OTA test solution is proposed herein. The cost can be reduced by more than an order of magnitude, while maintaining the test accuracy, as demonstrated below.

MIMO communications, where both the transmitting and receiving ports are equipped with multiple antennas, is a well-recognized approach to increase the spectral efficiency and the communication throughput [11]–[14]. The multi-antenna equipment enhances the communication reliability with antenna diversity, and transfers multiple data streams simultaneously in the same time–frequency window, which increases the communication capacity. Moreover, for massive MIMO communication, the base station can achieve very high (array) antenna gain through beam forming which allows for a substantial reduction in transmission power [1]. Hence, MIMO is a promising candidate technology that will be incorporated into 5G and beyond wireless communication systems.

OTA testing is a measurement method that can evaluate the true RF performance of an MIMO system. Sometimes, it is the only mean for accurate MIMO evaluations. First, OTA is conducted without cables connected to the device under test (DUT), namely, the DUT is evaluated under its normal operating conductions [15]–[17]. Further, for 5G and millimeter-wave (mmWave) systems, there may have no room to fit RF connectors for test purposes due to the small physical size and low cost requirement of the device, especially for chipset antennas [18], [19].

Manuscript received October 12, 2018; revised December 13, 2018; accepted January 21, 2019. Date of publication March 18, 2019; date of current version July 1, 2019. This work was supported in part by the Chinese Ministry of Education–China Mobile Research Foundation under Grant MCM 20150101 and in part by the National Natural Science Foundation of China under Grant 61671203. *(Corresponding author: Yihong Qi.)*

P. Shen is with the College of Electric and Information, Hunan University, Changsha 410082, China, and also with General Test Systems Inc., Shenzhen 518000, China (e-mail: penghui.shen@generaltest.com).

Y. Qi is with the College of Electric and Information, Hunan University, Changsha 410082, China, with General Test Systems Inc., Shenzhen 518000, China, and also with the EMC Laboratory, Missouri University of Science and Technology, Rolla, MO 65409 USA (e-mail: yihong. qi@generaltest.com).

W. Yu is with General Test Systems Inc., Shenzhen 518000, China (e-mail: fred.yu@generaltest.com).

J. L. Drewniak is with the Electromagnetic Compatibility Laboratory, Department of Electrical and Computer Engineering, Missouri University of Science and Technology, Rolla, MO 65409 USA (e-mail: drewniak@mst.edu).

M. Yu is with the Department of Electronic Engineering, Chinese University of Hong Kong, Hong Kong (e-mail: ming.yu@ieee.org).

F. Li is with the College of Electric and Information, Hunan University, Changsha 410082, China (e-mail: fuhai-li@vip.sina.com).

Color versions of one or more of the figures in this paper are available online at http://ieeexplore.ieee.org.

Digital Object Identifier 10.1109/TMTT.2019.2901687

MIMO communications take advantage of multipath propagation to improve the channel capacity. So the multipath channel properties should be characterized during MIMO OTA measurements. Two standard test methodologies for creating the spatial channel models are presented in the standard specifications: multiple probe anechoic chamber (MPAC) methods and the radiated two stage (RTS) method [20]–[22]. The RTS method is also denoted as a "wireless cable method" or "virtual cable method" [23], [24].

The standardizations for MIMO OTA have helped 4G long-term evolution (LTE) to enhance the entire network stability and increase the throughput. However, there still remains a potential challenge, which may fundamentally prevent the OTA test methodologies being adopted for 5G wireless evaluations. According to the standards [7]–[9], [25], all OTA measurement chambers are required to meet the far-field test conditions, namely, the test distance R should meet the requirements $R > 2D^2/\lambda$, $R > 3D$, and $R > 3\lambda$, where D is the total DUT dimension, and λ denotes the wavelength. So a certification chamber covering all the 4G cellular frequency bands (from 0.6 to 6 GHz) should be larger than 3.6 m for handling the DUTs of 0.3 m in size (the minimum quiet zone required in CTIA test plan [9] for holding cellular phones and head/hand phantoms). For a MPAC chamber for 4G MIMO, the size is usually larger than 7.2 m, since the test distance corresponds to the chamber radius [20], [23]. And the new progress of the MPAC method for 5G MIMO OTA testing is updated in [26].

The real challenges lie in the fact that 5G communication systems are generally working at higher frequency in terms of carrier. Proposals [25], [27] show that the frequency of 5G wireless terminals is up to 52.6 GHz, which corresponds to the far-field distance of dozens of meters for maintaining a 0.3-m-diameter quiet zone. Achieving far-field test conditions through a sizeable facility will result in high testing costs for 5G user equipment evaluations.

To address this issue, a compact size measurement system for MIMO OTA is proposed based on the RTS technique [21], [22], which is one of the standards [7], [8]. The RTS method has the advantage that the antenna pattern measurement is separated from throughput test. This makes it possible for a compact near-field chamber MIMO measurement. Then, for acquiring the far-field antenna pattern, the near-field to far-field transformation is used. In this paper, a source reconstruction algorithm is employed for reconstructing the far-field antenna pattern in the developed MIMO OTA test methodology [28]–[31]. Finally, MIMO throughput tests are conducted by utilizing the signals derived with combining the calculated far-field antenna pattern and the desired channel model. It is the first time the RTS method involving a transformation matrix is used for MIMO throughput evaluations.

The proposed compact size solution using a near-field to far-field transformation (RTS) significantly reduces the test distance for MIMO OTA, especially for 5G. The chamber dimension is only 1.9, as demonstrated herein, which can fit in ordinary office spaces and be easily relocatable. Compared to a far-field system, a reduction in the cost by at least an order of magnitude can be achieved without losing the test accuracy. The proposed compact solution is a promising candidate for 5G user equipment measurement standardization.

The RTS-based near-field test theory fundamentals are detailed in Section II, followed by the implementations of the proposed technique in a compact test system in Section III. In Section IV, the theory is compared with experiments, and, finally, the conclusions are presented.

II. RTS-Based Near-Field Testing

For MIMO OTA measurements, two standard methods, MPAC and RTS, are specified by the 3GPP and CTIA [7], [8]. The MPAC method uses multiple antennas surrounding the test zone for simulating the angles of arrival in all directions defined in the channel model [7], [20]. The multiple antenna environments, equipped with a multichannel emulator for real-time channel model emulation, generate the desired radiation environment.

The RTS method is implemented based on a first stage of DUT antenna pattern acquisition (including the amplitude and phase information at all directions), and followed by a second stage of throughput measurement via delivering the test vectors (consisting of the measured pattern and the desired channel model information) into the DUT receivers directly, in a radiated way. The conventional standard RTS method is conducted with far-field antenna pattern measurements.

Overcoming the far-field test limitation in antenna pattern measurements allows for a much shorter measurement distance. The proposed RTS-based near-field test method for MIMO OTA is on near-field to far-field transformation for achieving the antenna pattern in the method. In this paper, the far-field transformation is realized though the source reconstruction method, which exploits a group of electric and magnetic dipole moments to replace the real DUT in producing the same far-field antenna pattern. Then, finally the throughput is measured with far-field pattern information combined with channel emulation. The details of the theory are divided into three parts: first the MIMO OTA test theory, followed by the source reconstruction methodology, and finally, the RTS-based near-field throughput test algorithm.

A. MIMO OTA Test Theory

Multiple data streams are transmitted simultaneously in MIMO base station. And the MIMO user equipment recovers the transmitted streams from the received signals depending on the estimations of the propagation channel matrix [8]. So the behavior of the propagation environment plays a significant role in determining the throughput. The 3GPP has provided several standard channel models for modeling the typical use scenarios of MIMO user equipment, including the number of clusters, number of subpaths in each cluster, angles of departure, angles of arrivals, power distribution, and delay, Doppler frequency component, as shown in Fig. 1 [32], [33].

Based on the proposed channel models in [33], for a $P \times D$ MIMO system (with P antennas at base station side and D antennas at DUT side), the signal from the pth transmitting port to the dth receiving port (antenna feed) can be

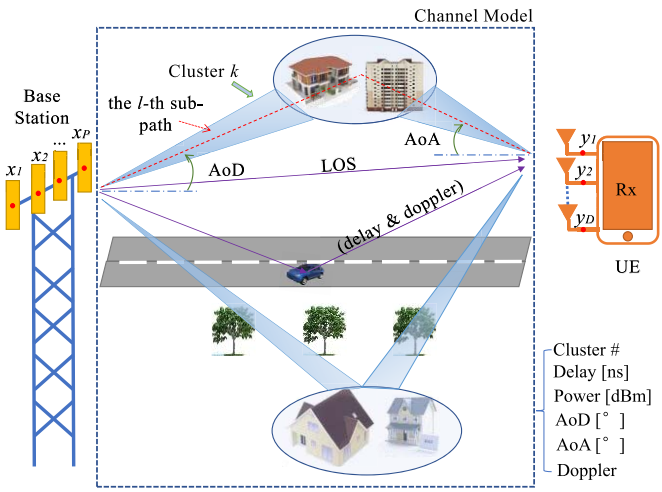

Fig. 1. Multipath channel model illustrations for MIMO.

processed as

$$h_{d,p}(t) = \sum_{l=1}^{L} e^{(j2\pi\Phi_l t + \psi_l + (-j2\pi f \tau_l))} \begin{bmatrix} G^V_{d,\mathrm{DUT}}(\alpha_{l,\mathrm{AoA}}) \\ G^H_{d,\mathrm{DUT}}(\alpha_{l,\mathrm{AoA}}) \end{bmatrix}^T \times \begin{bmatrix} \chi_l^{V,V} & \chi_l^{V,H} \\ \chi_l^{H,V} & \chi_l^{H,H} \end{bmatrix} \times \begin{bmatrix} G^V_{p,\mathrm{BS}}(\beta_{l,\mathrm{AoD}}) \\ G^H_{p,\mathrm{BS}}(\beta_{l,\mathrm{AoD}}) \end{bmatrix} \quad (1)$$

where L is the total number of subpaths over all clusters, Φ_l, ψ_l, and τ_l are the Doppler frequency component, prime phase, and delay of the lth subpath, respectively, $G^x_{d,\mathrm{DUT}}$ and $G^x_{p,BS}$ are the dth antenna gain of DUT and the pth antenna gain of base station in x polarization separately, $\alpha_{l,\mathrm{AoA}}$, $\beta_{l,\mathrm{AoD}}$, and $\chi_l^{x,y}$ represent the angle of arrival, angle of departure, and complex path loss from y polarization to x polarization of the lth subpath, respectively.

Then, the relationships between the P transmitted signals $(x_1, x_2, \ldots, x_P)$ and the D received signals $(y_1, y_2, \ldots, y_D)$ are

$$y(t) = \begin{bmatrix} h_{1,1}(t) & \cdots & h_{1,P}(t) \\ \vdots & \ddots & \vdots \\ h_{D,1}(t) & \cdots & h_{D,P}(t) \end{bmatrix} x(t) \quad (2)$$

where $y(t)$ and $x(t)$ mean the received vector $(y_1, y_2, \ldots, y_D)$ and the transmitting vector $(x_1, x_2, \ldots, x_P)$, respectively.

Assume that

$$H(t) = \begin{bmatrix} h_{1,1}(t) & \cdots & h_{1,P}(t) \\ \vdots & \ddots & \vdots \\ h_{D,1}(t) & \cdots & h_{D,P}(t) \end{bmatrix} \quad (3)$$

is the time-variant channel frequency response between the user equipment receivers and the base station antenna feeds, and the defined channel coefficient matrix in MIMO. Recovery of the original vector $x(t)$ uses the inverse of the coefficient matrix H. The accuracy is associated with the matrix condition number, the signal-to-noise ratio of the received signal $y(t)$, and the ability of the wireless terminal to accurately estimate the channel correlation matrix.

The RTS method is implemented based on the principle that the DUT antenna pattern, if known (or measured), with the standard base station antenna pattern, can be mathematically embedded into the channel model for the channel coefficient matrix real-time simulations. A simplified diagram for the RTS method is shown in Fig. 2, where the base station is used to generate the modulated signals, the channel emulator is utilized to mimic the H matrix through integrating the base station antenna pattern, the channel property, and the user equipment antenna pattern, as given in (1)–(3). The channel emulator output vectors, which should be delivered into the user equipment receiver input ports without crosscoupling, are indeed transferred separately via "virtual links." It is worth noting that similar to the real RF cables, the virtual links deliver signals directly and without crosscoupling, and, no real RF connections on the DUT are required, as stated below.

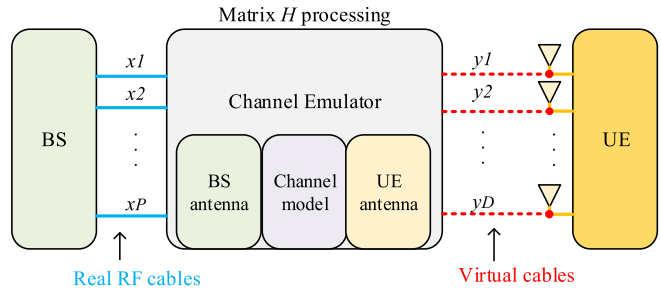

Fig. 2. Simplified diagram for the RTS system.

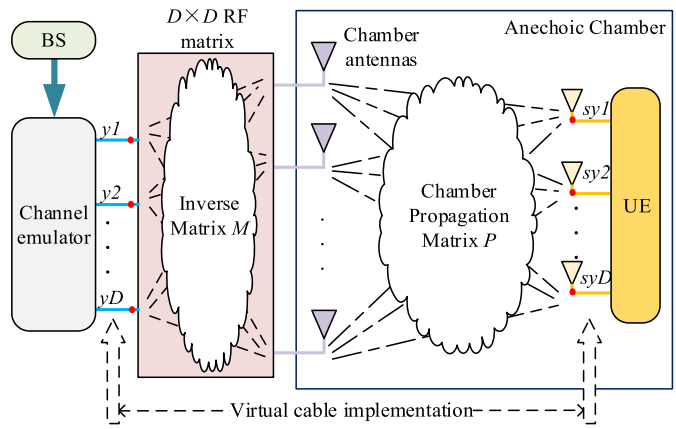

Fig. 3. Virtual cable technique.

In the RTS test, the DUT is fixed in the chamber, as illustrated in Fig. 3, where the D channel emulator output signals $(y_1, y_2, \ldots, y_D)$ are fed to the D chamber antennas after passing a $D \times D$ RF processing module (recorded as matrix M). The propagation scenario from the D chamber antennas to D DUT receivers can be regarded as a $D \times D$ matrix (marked as the chamber propagation matrix P), mathematically. Once setting matrix M being the inverse of P, the DUT receiver inputs can be accessed by the channel emulator outputs directly, similar as the real RF cable does, as

$$\begin{aligned}(sy_1, sy_2, \ldots, sy_D)^T &= P \times M \times (y_1, y_2, \ldots, y_D)^T \\ &= (y_1, y_2, \ldots, y_D)^T \end{aligned} \quad (4)$$

where $(\ )^T$ denotes the transpose. Thus, this approach is called the "virtual link" method [13]. With this virtual link

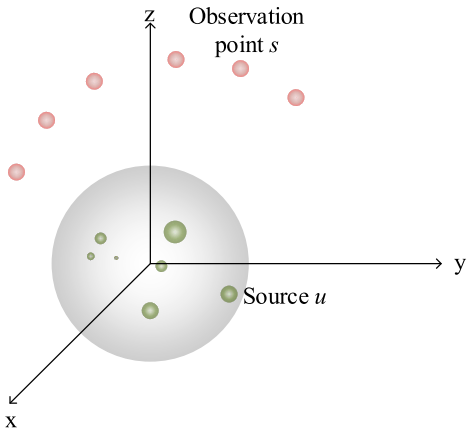

Fig. 4. U dipole moments inside a sphere and S observation points outside.

established, the user equipment is evaluated in OTA mode, resulting that the results are the correct reflections of DUT's real user experience.

B. Source Reconstruction

A finite size radiation source may be replaced by an equivalent multipole expansion which gives the same radiation pattern as the real source [34]. Under appropriate division, the volume of the radiation source can be split into several electrically small dimensions, which can be replaced by a dipole moment with three electric components along the xyz axes (denoted by Q_x, Q_y, Q_z) and three magnetic components along the xyz axes (denoted by M_x, M_y, M_z).

Fig. 4 shows U dipole moments inside a sphere and S observation points outside the spherical boundary. The observed electric fields at the sth point contributed by the uth source can be characterized as [35]

$$\begin{aligned} E_{x,s,u} &= \begin{pmatrix} -jk_o\eta_o G\left(1-\frac{1}{(k_oR)^2}-\frac{j}{k_oR}\right) \\ -jk_o\eta_o G\left(\frac{3}{(k_oR)^2}+\frac{3j}{k_oR}-1\right)\frac{(x-x')^2}{R^2} \end{pmatrix} Q_{x,u} \\ &\quad - jk_o\eta_o G\left(\frac{3}{(k_oR)^2}+\frac{3j}{k_oR}-1\right)\frac{(x-x')(y-y')}{R^2}Q_{y,u} \\ &\quad - jk_o\eta_o G\left(\frac{3}{(k_oR)^2}+\frac{3j}{k_oR}-1\right)\frac{(x-x')(z-z')}{R^2}Q_{z,u} \\ &\quad - k_o^2 G\left(\frac{1}{(k_oR)^2}+\frac{j}{k_oR}\right)(z-z')M_{y,u} \\ &\quad + k_o^2 G\left(\frac{1}{(k_oR)^2}+\frac{j}{k_oR}\right)(y-y')M_{z,u} \end{aligned} \tag{5}$$

$$\begin{aligned} E_{y,s,u} &= -jk_o\eta_o G\left(\frac{3}{(k_oR)^2}+\frac{3j}{k_oR}-1\right)\frac{(x-x')(y-y')}{R^2}Q_{x,u} \\ &\quad - \begin{pmatrix} jk_o\eta_o G\left(1-\frac{1}{(k_oR)^2}-\frac{j}{k_oR}\right) \\ +jk_o\eta_o G\left(\frac{3}{(k_oR)^2}+\frac{3j}{k_oR}-1\right)\frac{(y-y')^2}{R^2} \end{pmatrix} Q_{y,u} \\ &\quad - jk_o\eta_o G\left(\frac{3}{(k_oR)^2}+\frac{3j}{k_oR}-1\right)\frac{(y-y')(z-z')}{R^2}Q_{z,u} \\ &\quad + k_o^2 G\left(\frac{1}{(k_oR)^2}+\frac{j}{k_oR}\right)(z-z')M_{x,u} \\ &\quad - k_o^2 G\left(\frac{1}{(k_oR)^2}+\frac{j}{k_oR}\right)(x-x')M_{z,u} \end{aligned} \tag{6}$$

$$\begin{aligned} E_{z,s,u} &= -jk_o\eta_o G\left(\frac{3}{(k_oR)^2}+\frac{3j}{k_oR}-1\right)\frac{(x-x')(z-z')}{R^2}Q_{x,u} \\ &\quad - jk_o\eta_o G\left(\frac{3}{(k_oR)^2}+\frac{3j}{k_oR}-1\right)\frac{(y-y')(z-z')}{R^2}Q_{y,u} \\ &\quad - \begin{pmatrix} jk_o\eta_o G\left(1-\frac{1}{(k_oR)^2}-\frac{j}{k_oR}\right) \\ +jk_o\eta_o G\left(\frac{3}{(k_oR)^2}+\frac{3j}{k_oR}-1\right)\frac{(z-z')^2}{R^2} \end{pmatrix} Q_{z,u} \\ &\quad - k_o^2 G\left(\frac{1}{(k_oR)^2}+\frac{j}{k_oR}\right)(y-y')M_{x,u} \\ &\quad + k_o^2 G\left(\frac{1}{(k_oR)^2}+\frac{j}{k_oR}\right)(x-x')M_{y,u} \end{aligned} \tag{7}$$

where $Q_{x,u}, Q_{y,u}, Q_{z,u}$ and $M_{x,u}, M_{y,u}, M_{z,u}$ are the electric and magnetic components along the xyz directions of the uth source at the location (x', y', z'), respectively, $E_{x,s,u}, E_{y,s,u}$, and $E_{z,s,u}$ are the observed electric field components at the sth observation [corresponding the location (x, y, z)] contributed by the uth source along the xyz axes, k_o and η_o are the wavenumber and impedance, respectively, and G and R are

$$\begin{aligned} G &= \frac{e^{-jk_oR}}{4\pi R} \\ R &= \sqrt{(x-x')^2+(y-y')^2+(z-z')^2}. \end{aligned} \tag{8}$$

Rewrite (5)–(7) as

$$\begin{aligned} E_{x,s,u} &= \mathcal{X}_{x,x}^{s,u}\times Q_{x,u} + \mathcal{X}_{x,y}^{s,u}\times Q_{y,u} + \mathcal{X}_{x,z}^{s,u}\times Q_{z,u} \\ &\quad + \psi_{x,y}^{s,u}\times M_{y,u} + \psi_{x,z}^{s,u}\times M_{z,u} \end{aligned} \tag{9}$$

$$\begin{aligned} E_{y,s,u} &= \mathcal{X}_{y,x}^{s,u}\times Q_{x,u} + \mathcal{X}_{y,y}^{s,u}\times Q_{y,u} + \mathcal{X}_{y,z}^{s,u}\times Q_{z,u} \\ &\quad + \psi_{y,x}^{s,u}\times M_{x,u} + \psi_{y,z}^{s,u}\times M_{z,u} \end{aligned} \tag{10}$$

$$\begin{aligned} E_{z,s,u} &= \mathcal{X}_{z,x}^{s,u}\times Q_{x,u} + \mathcal{X}_{z,y}^{s,u}\times Q_{y,u} + \mathcal{X}_{z,z}^{s,u}\times Q_{z,u} \\ &\quad + \psi_{z,x}^{s,u}\times M_{x,u} + \psi_{z,y}^{s,u}\times M_{y,u}. \end{aligned} \tag{11}$$

$E_{x,s,u}$, $E_{y,s,u}$ and $E_{z,s,u}$ are related to $Q_{x,u}, Q_{y,u}, Q_{z,u}, M_{x,u}, M_{y,u}, M_{z,u}$ as

$$\begin{aligned} \begin{bmatrix} E_{x,s,u} \\ E_{y,s,u} \\ E_{z,s,u} \end{bmatrix} &= \begin{bmatrix} \mathcal{X}_{x,x}^{s,u} & \mathcal{X}_{x,y}^{s,u} & \mathcal{X}_{x,z}^{s,u} & 0 & \psi_{x,y}^{s,u} & \psi_{x,z}^{s,u} \\ \mathcal{X}_{y,x}^{s,u} & \mathcal{X}_{y,y}^{s,u} & \mathcal{X}_{y,z}^{s,u} & \psi_{y,x}^{s,u} & 0 & \psi_{y,z}^{s,u} \\ \mathcal{X}_{z,x}^{s,u} & \mathcal{X}_{z,y}^{s,u} & \mathcal{X}_{z,z}^{s,u} & \psi_{z,x}^{s,u} & \psi_{z,y}^{s,u} & 0 \end{bmatrix} \\ &\quad \times \begin{bmatrix} Q_{x,u} \\ Q_{y,u} \\ Q_{z,u} \\ M_{x,u} \\ M_{y,u} \\ M_{z,u} \end{bmatrix} \\ &= T_{s,u}\times QM_u \end{aligned} \tag{12}$$

where coefficients $T_{s,u}$ and QM_u are

$$T_{s,u} = \begin{bmatrix} \mathcal{X}_{x,x}^{s,u} & \mathcal{X}_{x,y}^{s,u} & \mathcal{X}_{x,z}^{s,u} & 0 & \psi_{x,y}^{s,u} & \psi_{x,z}^{s,u} \\ \mathcal{X}_{y,x}^{s,u} & \mathcal{X}_{y,y}^{s,u} & \mathcal{X}_{y,z}^{s,u} & \psi_{y,x}^{s,u} & 0 & \psi_{y,z}^{s,u} \\ \mathcal{X}_{z,x}^{s,u} & \mathcal{X}_{z,y}^{s,u} & \mathcal{X}_{z,z}^{s,u} & \psi_{z,x}^{s,u} & \psi_{z,y}^{s,u} & 0 \end{bmatrix}$$

$$QM_u = \begin{bmatrix} Q_{x,u} & Q_{y,u} & Q_{z,u} & M_{x,u} & M_{y,u} & M_{z,u} \end{bmatrix}^T. \quad (13)$$

Thus, for the sth observation, the total electric field contributed by all U sources (denoted by $E_{x,s}$, $E_{y,s}$, $E_{z,s}$) can be integrated as

$$\begin{bmatrix} E_{x,s} \\ E_{y,s} \\ E_{z,s} \end{bmatrix} = \sum_{u=1}^{U} (T_{s,u} \times QM_u) \quad (14)$$

which can be further expressed as

$$\begin{bmatrix} E_{x,s} \\ E_{y,s} \\ E_{z,s} \end{bmatrix} = \begin{bmatrix} T_{s,1} & T_{s,2} & \cdots & T_{s,U} \end{bmatrix} \begin{bmatrix} QM_1 \\ QM_2 \\ \vdots \\ QM_U \end{bmatrix}. \quad (15)$$

Rewrite $\begin{bmatrix} E_{x,s} \\ E_{y,s} \\ E_{z,s} \end{bmatrix}$ as $E_{o,s}$, and finally the electric fields at all observations associated with the all sources can be obtained as

$$\begin{bmatrix} E_{o,1} \\ E_{o,2} \\ \vdots \\ E_{o,S} \end{bmatrix} = \begin{bmatrix} T_{1,1} & T_{1,2} & \cdots & T_{1,U} \\ T_{2,1} & T_{2,2} & \cdots & T_{2,U} \\ \vdots & \vdots & \ddots & \vdots \\ T_{S,1} & T_{S,2} & \cdots & T_{S,U} \end{bmatrix} \begin{bmatrix} QM_1 \\ QM_2 \\ \vdots \\ QM_U \end{bmatrix}. \quad (16)$$

Re-express (16) as

$$\begin{bmatrix} E_{o,1} \\ E_{o,2} \\ \vdots \\ E_{o,S} \end{bmatrix} = T_{\mathrm{ET}} \begin{bmatrix} QM_1 \\ QM_2 \\ \vdots \\ QM_U \end{bmatrix}. \quad (17)$$

where T_{ET} is recorded as the generating matrix in the rest of this paper, which is a coefficient dependent upon the observation locations and the source coordinates.

Based on the observed electric field in (17), the sources can be constructed as

$$\begin{bmatrix} QM_1 \\ QM_2 \\ \vdots \\ QM_U \end{bmatrix} = \left(T_{\mathrm{ET}}^* T_{\mathrm{ET}}\right)^{-1} T_{\mathrm{ET}}^* \begin{bmatrix} E_{o,1} \\ E_{o,2} \\ \vdots \\ E_{o,S} \end{bmatrix}. \quad (18)$$

where $(\ )^*$ denotes the conjugate transpose.

C. RTS Algorithm with Near-field to Far-field Transformation Embebdded

The presented method is based on three steps: the DUT field measurement over a spherical surface in the near field, the near-field to far-field transformation, and the throughput test. Compared with the conventional RTS, which involves the measured far-field pattern into (1)–(3) directly, an additional transfer matrix is needed in the presented test process, as detailed below.

After the field measurement points being taken in the near field and selecting a set of appropriate locations for placing the U dipole moments, the generating matrix T_{ET} can be calculated according to (16) and (17). Then, knowing the observed electric field pattern and the generating matrix, the sources can be reconstructed through (18). Similarly, the generating matrix between the reconstructed dipoles and the desired far-field antenna pattern points can be computed and denoted as T_{ER}. Finally, the far-field electric field at the kth location, marked as $G_{o,k}$, is

$$G_{o,k} = T_{\mathrm{ER},k} \begin{bmatrix} QM_1 \\ QM_2 \\ \vdots \\ QM_U \end{bmatrix} \quad (19)$$

where $T_{\mathrm{ER},k}$ is the kth row of T_{ER}, $\begin{bmatrix} QM_1 \\ QM_2 \\ \vdots \\ QM_U \end{bmatrix}$ is the equivalent sources, and $G_{o,k}$ consists three components along xyz axes $G_{o,k} = \begin{bmatrix} G_{x,k} & G_{y,k} & G_{z,k} \end{bmatrix}^T$.

The far-field antenna gain obtained in (19) cannot be used in the channel coefficient matrix calculations, since the Cartesian coordinate is used in (19), while the spherical coordinate is applied in (1). Taking the kth location as an example, a conversion matrix is required for coordinate transformation from Cartesian to spherical as

$$\begin{bmatrix} G_{V,k} \\ G_{H,k} \end{bmatrix} = \begin{bmatrix} \cos\theta_k \cos\varphi_k & \cos\theta_k \sin\varphi_k & -\sin\theta_k \\ -sin\varphi_k & \cos\varphi_k & 0 \end{bmatrix} \begin{bmatrix} G_{x,k} \\ G_{y,k} \\ G_{z,k} \end{bmatrix} \quad (20)$$

where θ_k and φ_k are the related angle of the kth location in spherical coordinate, and $G_{V,k}$ and $G_{H,k}$ are the far-field antenna gain in the vertical and horizontal polarizations.

Assume that the kth location corresponds to the angle of arrival of $\alpha_{l,\mathrm{AoA}}$ in the channel model. Then, with the near-field to far-field algorithm embedded, the (d, p) component of the new channel coefficient matrix H is

$$h_{d,p}^{\mathrm{new}}(t) = \sum_{l=1}^{L} e^{(j2\pi\Phi_l t + \psi_l + (-j2\pi f \tau_l))} \begin{bmatrix} G_{V,k} \\ G_{H,k} \end{bmatrix}^T \times \begin{bmatrix} \chi_l^{V,V} & \chi_l^{V,H} \\ \chi_l^{H,V} & \chi_l^{H,H} \end{bmatrix} \times \begin{bmatrix} G_{p,BS}^V(\beta_{l,AoD}) \\ G_{p,BS}^H(\beta_{l,AoD}) \end{bmatrix} \quad (21)$$

Through (18)–(21), $h_{d,p}^{\mathrm{new}}(t)$ is associated with the near-field measured antenna gain as (22), shown at the bottom of the next page, where $\begin{bmatrix} E_{o,1} \\ E_{o,2} \\ \vdots \\ E_{o,S} \end{bmatrix}^T$ is the measured electric fields in the near field, and k and l are equivalent.

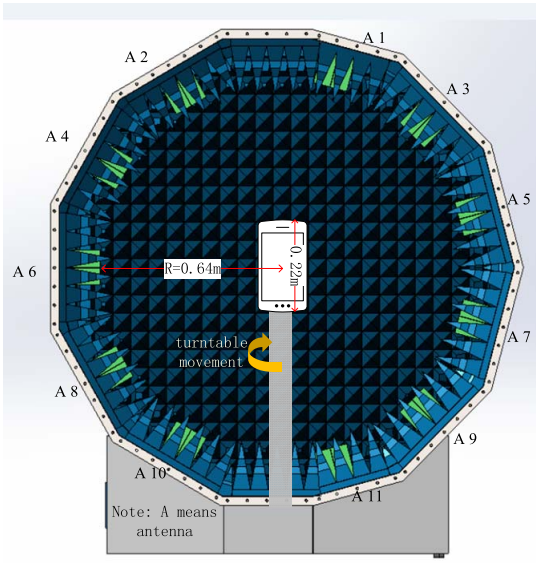

Fig. 5. Compact size chamber for MIMO.

Further, we can have the channel coefficient matrix in the near-field RTS method as

$$H^{\text{new}}(t) = \begin{bmatrix} h_{1,1}^{\text{new}}(t) & \cdots & h_{1,P}^{\text{new}}(t) \\ \vdots & \ddots & \vdots \\ h_{D,1}^{\text{new}}(t) & \cdots & h_{D,P}^{\text{new}}(t) \end{bmatrix}. \tag{23}$$

With loading the matrix $H^{\text{new}}(t)$ in the channel emulator, the last step for throughput testing can be conducted via virtual links in the near-field RTS test process.

III. Compact System for MIMO OTA

A compact size chamber for performing MIMO OTA test has been developed, as illustrated in Fig. 5, where eleven dual-polarization chamber antennas are arranged in a vertical ring, and the ith antenna (marked as Ai in Fig. 5) is placed at $\theta = 15 \times i$ degrees referred to the spherical coordinate of the system. The antenna layout, together with a turntable, achieves a minimum sampling interval of 15° in the theta direction, and 1° in phi. The outer chamber size is within 1.9 m × 1.8 m × 1.1 m ($H \times L \times W$). And the available measurement distance is approximately 0.64 m in consideration of the height of the chamber antennas and absorbers.

The distance clearly does not meet the far-field measurement requirements. Actually, in this paper, we will validate the accuracy of the compact size system within a user equipment of 0.22 m in dimension, at 3.8 GHz and at 751 MHz, which corresponds to a far-field test distance of 1.3 m at 3.8 GHz (determined by $R > 2D^2/\lambda$) and 1.2 m at 751 MHz (determined by $R > 3\lambda$). The far-field distance requirements are approximately two times larger than the compact size system in Fig. 5. The experiments and comparisons between the compact size system and a certified far-field measurement system are detailed below.

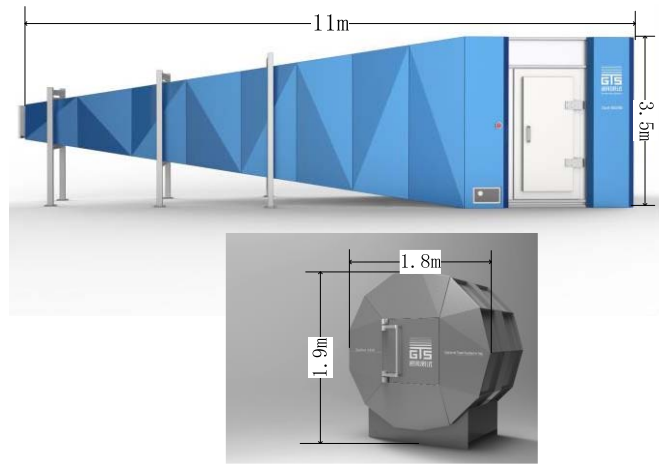

Fig. 6. Compact chamber (1.9 m × 1.8 m × 1.1 m) and the certification chamber (11 m × 3.5 m × 3.5 m).

IV. Experiments and Comparisons

A. Setups

A larger certification chamber with dimensions 11 m × 3.5 m × 3.5 m ($L \times H \times W$) in size is selected for comparisons, as shown in Fig. 6. A horn antenna and a two-axis turntable are equipped in the huge chamber for performing 3-D measurements, and the test distance inside is approximately 9.5 m. The setups are listed in Table I. The measurement procedure is comprised of two steps. First, measure the antenna patterns in the compact size chamber and conduct throughput tests based on the new near-field RTS method. Second, carry out pattern and throughput tests based on the standard RTS method in the huge chamber (without near-field to far-field transformation). Finally, the results can be compared. In both steps, after achieving the far-field patterns, the throughput test is carried out by selecting two measurement probes and delivering the throughput test signals into the DUT receivers via virtual links [15], [21], [24].

Theoretically, the compact chamber size is not limited. However, in practice, the compact solution in this paper has limitations on physical dimensions. First, the DUT is placed in chamber quiet zone during testing, where the reflection

$$h_{d,p}^{\text{new}}(t) = \sum_{l,k=1}^{L} \left(\begin{bmatrix} E_{o,1} \\ E_{o,2} \\ \vdots \\ E_{o,S} \end{bmatrix}^T \left(\begin{bmatrix} \cos\theta_k \cos\varphi_k & \cos\theta_k \sin\varphi_k & -\sin\theta_k \\ -\sin\varphi_k & \cos\varphi_k & 0 \end{bmatrix} T_{\text{ER},k} \left(T_{\text{ET}}^* T_{\text{ET}}\right)^{-1} T_{\text{ET}}^* \right)^T \cdot \begin{bmatrix} \chi_l^{V,V} & \chi_l^{V,H} \\ \chi_l^{H,V} & \chi_l^{H,H} \end{bmatrix} \begin{bmatrix} G_{p,BS}^V(\beta_{l,AoD}) \\ G_{p,BS}^H(\beta_{l,AoD}) \end{bmatrix} e^{(j2\pi\Phi_l t + \psi_l + (-j2\pi f \tau_l))} \right) \tag{22}$$

TABLE I
MEASUREMENT PARAMETERS

Parameters	Value
Test item	2×2 MIMO throughput
Instruments	Vector network analyzer, Keysight E7515A (UXM),
Smart anechoic chamber	RayZone 1800 from General Test Systems Inc. (GTS) [36]
Certification chamber	Dart 9000B from GTS [36]
Test frequency	751 MHz 3.8 GHz
Channel model	SCME Uma

levels are controlled so that the measurement accuracy is not compromised. The CTIA and 3GPP test standards [7] and [9] have specified the requirements of the quiet zone, which is related to the test distance. So the quiet zone is a concern in a compact test system. Second, in the proposed compact solution, eleven measurement probes are integrated in one small chamber. The crosscoupling between any two antennas are also associated with the chamber size. The smaller the chamber, the larger is the crosscoupling. Hence, the two mentioned factors should be considered in practical test systems.

B. Comparisons and Analysis

The antenna patterns determined under the two conditions are compared, as shown in Fig. 7(a) of gain patterns and Fig. 7(b) of relative phase patterns (for 751 MHz), and Fig. 8(a) of gain patterns and Fig. 8(b) of relative phase patterns (for 3.8 GHz), where the blue lines denote the measured patterns in the compact chamber, the red lines are the reconstructed patterns in the far-field from the near-field measurements, the black curves represent the measured results in far-field, AIR0 and AIR1 are the main antenna and the sub antenna in user equipment, respectively, and V and H denote the polarizations. The comparisons show that at low frequency, the calculated far-field patterns have correlate with the far-field measurement results, and the difference in the direction of primary gain is approximately 0.5 dB. However, in the 3.8-GHz high-frequency case, the difference in the direction of primary gain reaches 1.5 dB. The errors may be caused by several factors.

The path-loss and phase calibrations can be a source of error. In the large chamber, the calibration accuracy is primarily determined by the gain ripples of the calibration antennas (diploe and loop). While in the compact system, besides the ripples, the common mode current radiations along the conducted cables may impact the gain and phase calibrations since the cables are in proximity to the chamber antennas (especially the A10 and A11 in Fig. 5). Moreover, the position offset would contribute a larger calibration uncertainty in a smaller system.

Another source of error is the observation coordinate accuracy. In the source reconstruction process, the observation location information is required, as derived in (5)–(7), where xyzcorrespond to the observation coordinates. In this paper, we acquire the near-field observed electric fields in the compact chamber equipped with 11 measurement antennas.

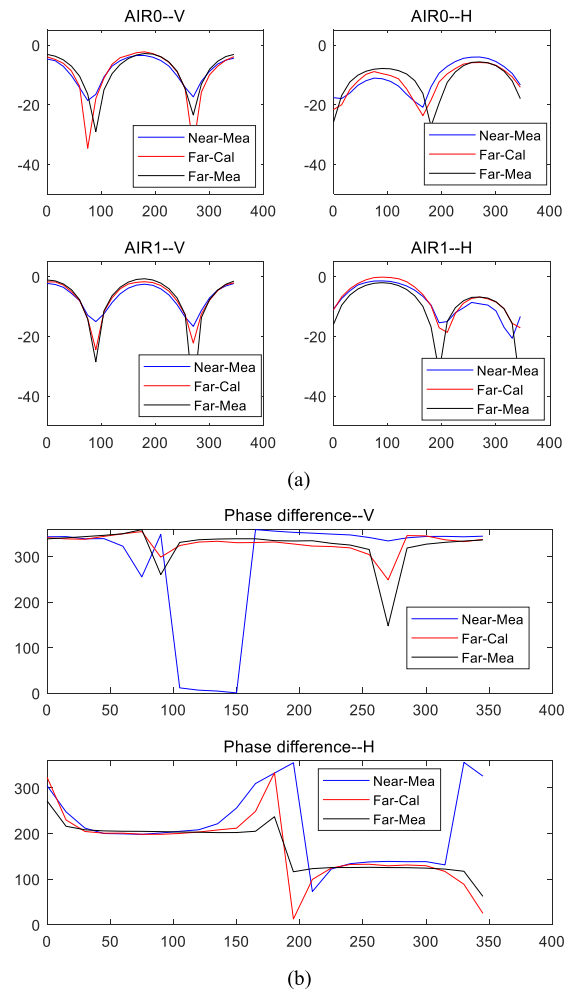

Fig. 7. (a) Gain pattern comparisons at 751 MHz. (b) Relative phase pattern comparisons at 751 MHz.

Theoretically, the 11 measurement antennas are located on a circle with the same radius, as shown in Fig. 5. Namely, the observations are located on a spherical surface. However, at least two factors in practice impact the observation positions. The first one is the consistency of the 11 chamber antennas. All the measurement antenna phase centers are required to be the same or calibrated carefully, so that the observation positions can be calculated accurately. The second one lies on the fact that all the antennas are installed with microwave absorbers surrounded nearby, which can impact the antenna radiation and the phase center. Finally, the phase centers are almost impossible to evaluate accurately considering the installation inside such a small system.

Finally, the computing errors of observation coordinate have a lager influence on far-field pattern calculations at high frequency. The higher the frequency, the larger will be the phase measurement errors due to the physical location offsets.

The throughput results using the near-field RTS-based method in a compact size system are compared with the standard RTS method in a full-scale certification chamber in Fig. 9. The throughput results between the certification chamber and the compact system (with near-field tofar-field technique), differ by approximately 0.5 dB in both bands. It is worth noting that according to the standards [7] and [9], the difference between different labs may be larger

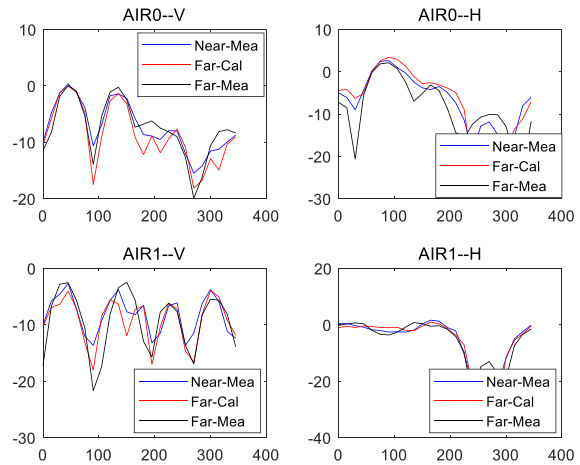

(a)

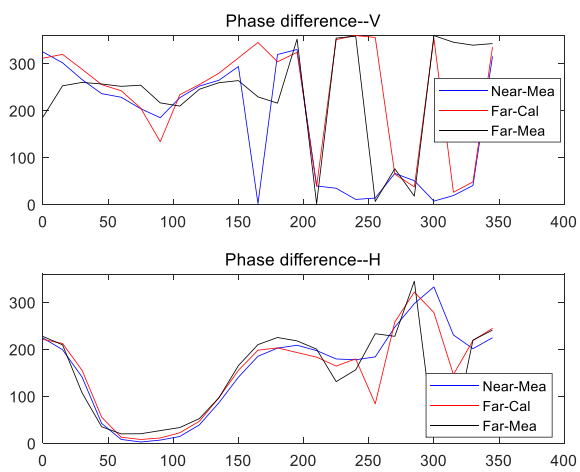

(b)

Fig. 8. (a) Gain pattern comparisons at 3.8 GHz. (b) Relative phase pattern comparisons at 3.8 GHz.

than 2.65 dB. Actually, a report showed that for three MPAC systems, the test difference between different labs could reach 7.31 dB [37]. In the present case, the results in the compact size chamber and the full-scale certification chamber are very comparable. The differences between the antenna patterns seem larger than the throughput, because the throughput results are acquired through averaging the performance over all angles.

Both the antenna reconstructions and the throughput are validated in this section. The results validate the compact solution are critical to the feasibility demonstration of the compact solution.

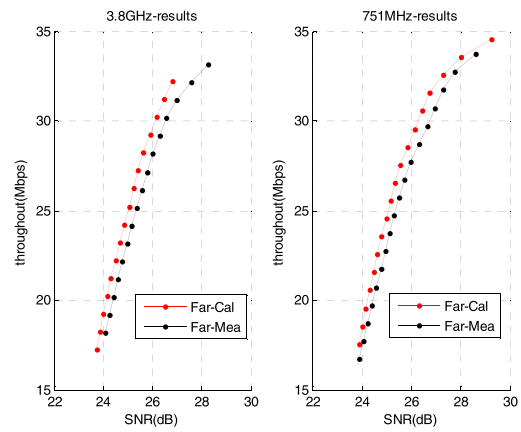

Fig. 9. Throughput comparisons.

C. Measurement Uncertainty Analysis

The conventional RTS method implemented in the far-field is one of the MIMO OTA test standards specified by the 3GPP, and the measurement uncertainties were discussed in [7] and [11]. Different from the standard RTS, the far-field patterns are obtained through near-field to far-field transformation in the compact solution in this paper. Therefore, in this part, two additional measurement uncertainties are discussed, which are mainly contributed by the antenna pattern processing

The far-field antenna patterns are derived by combining the source reconstruction technique with the near-field measurements. So the uncertainty may lie primarily with two factors. The first one is the antenna pattern measurement errors in the near field. Considering the measurement errors in magnitude and phase, the (d, p) component of the practical measured and applied channel coefficient matrix described in (23), where $\begin{bmatrix} R|E_{o,1} \\ R|E_{o,2} \\ \vdots \\ R|E_{o,S} \end{bmatrix}$ is the practical measured antenna patterns in near field with uncertainties included, which is related to the accurate value $\begin{bmatrix} E_{o,1} \\ E_{o,2} \\ \vdots \\ E_{o,S} \end{bmatrix}$ [detailed in formula (22)] as

$$\begin{bmatrix} R|E_{o,1} \\ R|E_{o,2} \\ \vdots \\ R|E_{o,S} \end{bmatrix} = E_d * e^{j\varphi_d} \begin{bmatrix} E_{o,1} \\ E_{o,2} \\ \vdots \\ E_{o,S} \end{bmatrix} \tag{25}$$

$$R|h_{d,p}^{\text{new}}(t) = \sum_{l,k=1}^{L} \left(\begin{bmatrix} R|E_{o,1} \\ R|E_{o,2} \\ \vdots \\ R|E_{o,S} \end{bmatrix}^T \left(\begin{bmatrix} \cos\theta_k \cos\varphi_k & \cos\theta_k \sin\varphi_k & -\sin\theta_k \\ -\sin\varphi_k & \cos\varphi_k & 0 \end{bmatrix} T_{\text{ER},k} \left(T_{\text{ET}}^* T_{\text{ET}}\right)^{-1} T_{\text{ET}}^* \right)^T \cdot \begin{bmatrix} \chi_l^{V,V} & \chi_l^{V,H} \\ \chi_l^{H,V} & \chi_l^{H,H} \end{bmatrix} \begin{bmatrix} G_{p,BS}^V(\beta_{l,AoD}) \\ G_{p,BS}^H(\beta_{l,AoD}) \end{bmatrix} e^{(j2\pi\Phi_l t + \psi_l + (-j2\pi f \tau_l))} \right) \tag{24}$$

where $E_d \times e^{j\varphi_d}$ is the pattern measurement error of the dth antenna.

From (22) and (23), and (24), shown at the bottom of the previous page, we can have that

$$R|h_{d,p}^{\text{new}}(t) = E_d \times e^{j\varphi_d} \times h_{d,p}^{\text{new}}(t). \tag{26}$$

Then, the practical applied channel coefficient matrix (marked as $R|H^{\text{new}}(t)$) is

$$\begin{aligned} R|H^{\text{new}}(t) &= \begin{bmatrix} E_1 \times e^{j\varphi_1} & \cdots & 0 \\ \vdots & \ddots & \vdots \\ 0 & \cdots & E_D \times e^{j\varphi_D} \end{bmatrix} \begin{bmatrix} h_{1,1}^{\text{new}}(t) & \cdots & h_{1,P}^{\text{new}}(t) \\ \vdots & \ddots & \vdots \\ h_{D,1}^{\text{new}}(t) & \cdots & h_{D,P}^{\text{new}}(t) \end{bmatrix} \\ &= \begin{bmatrix} E_1 \times e^{j\varphi_1} & \cdots & 0 \\ \vdots & \ddots & \vdots \\ 0 & \cdots & E_D \times e^{j\varphi_D} \end{bmatrix} \times H^{\text{new}}(t). \end{aligned} \tag{27}$$

Following the derivations [from formula (16) to formula (32)] in [11], this kind of error can also be minimized, and would not impact the MIMO throughput tests.

Another contributor of uncertainty is the observation coordinate calculation. As stated before, the observation computing errors (marked as ΔR) would be introduced into the near-field-to-far-field transformation, and impact the far-field antenna patterns. The higher the frequency, the larger the phase measurement error caused by the ΔR, the lower the pattern rebuilding accuracy. The relationship between the ΔR and the pattern reconstruction errors is required to be validated carefully, which is another topic for future research.

V. Conclusion

A compact measurement solution for 5G MIMO OTA evaluations is reported in this paper, where for the first time the RTS method embedding a transformation matrix is applied. Overcoming the direct far-field measurement scenario dramatically reduces the test distance. This solution significantly reduces test expenses, compared with full-scale MIMO OTA test systems, and without losing the measurement accuracy. Considering that there are two standard MIMO OTA test methods (RTS and MPAC) for 4G, the RTS approach with the near-field-to-far-field transformation integrated can realize throughput evaluations in a compact size system, which is also one of its unique advantages. Hence, the proposed solution is a promising candidate for 5G terminal measurement standardizations.

On the other hand, for a limited size OTA measurement system, the bigger the DUT, the larger will be the measurement errors. These errors are not readily quantifiable. Therefore, the proposed near-field-to-far-field transformation-based RTS test method eliminates the measurement distance-related errors so that the MIMO OTA test can be performed in a more compact and cost-effective chamber.

Finally, although lacking 5G high-frequency validations (caused by lacking the terminals), experiments are performed in the bands of 751 MHz and 3.8 GHz (4G LTE and 5G frequency range 1), which further demonstrate this new near-field solution for 5G.

References

[1] H. Q. Ngo, *Massive MIMO: Fundamentals and System Designs*. Linköping, Sweden: LiU-Tryck, 2015.

[2] B. Yang, Z. Yu, J. Lan, R. Zhang, J. Zhou, and W. Hong, "Digital beamforming-based massive MIMO transceiver for 5G millimeter-wave communications," *IEEE Trans. Microw. Theory Techn.*, vol. 66, no. 7, pp. 3403–3418, Jul. 2018.

[3] Y. Kim *et al.*, "Full dimension MIMO (FD-MIMO): The next evolution of MIMO in LTE systems," *IEEE Wireless Commun.*, vol. 21, no. 2, pp. 26–33, Apr. 2014.

[4] M. Samimi and T. S. Rappaport, "3-D millimeter-wave statistical channel model for 5G wireless system design," *IEEE Trans. Microw. Theory Techn.*, vol. 64, no. 7, pp. 2207–2225, Jul. 2016.

[5] Y. Qi *et al.*, "5G over-the-air measurement challenges: Overview," *IEEE Trans. Electromagn. Compat.*, vol. 59, no. 6, pp. 1661–1670, Dec. 2017.

[6] K. N. R. S. V. Prasad, E. Hossain, and V. K. Bhargava, "Energy efficiency in massive MIMO-based 5G networks: Opportunities and challenges," *IEEE Wireless Commun.*, vol. 24, no. 3, pp. 86–94, Jun. 2017.

[7] "User equipment (UE) over the air (OTA) performance; Conformance testing," 3GPP, Tech. Rep. Specif. TS 37.544 v14.5.0, 2018.

[8] *Test Plan for 2 × 2 Downlink MIMO and Transmit Diversity Over-the-Air Performance*, document Revision 1.1, CTIA, Washington, DC, USA, Aug. 2016.

[9] *Test Plan for Mobile Station Over the Air Performance*, document Revision 3.3.5, CTIA, Washington, DC, USA, Jul. 2016.

[10] T. W. Nuteson, M. B. Steer, S. Nakazawa, and J. W. Mink, "Near-field and far-field prediction of quasi-optical grid arrays," *IEEE Trans. Microw. Theory Techn.*, vol. 47, no. 1, pp. 6–13, Jan. 1999.

[11] X. Liu *et al.*, "Beam-oriented digital predistortion for 5G Massive MIMO hybrid beamforming transmitters," *IEEE Trans. Microw. Theory Techn.*, vol. 66, no. 7, pp. 3419–3432, Jul. 2018.

[12] Y. Jing, H. Kong, and M. Rumney, "MIMO OTA test for a mobile station performance evaluation," *IEEE Instrum. Meas. Mag.*, vol. 19, no. 3, pp. 43–50, Jun. 2016.

[13] P. Shen, Y. Qi, W. Yu, and F. Li, "Eliminating RSARP reporting errors in the RTS method for MIMO OTA test," *IEEE Trans. Electromagn. Compat.*, vol. 59, no. 6, pp. 1708–1715, Dec. 2017.

[14] S. Yang, C. Zhou, T. Lv, and L. Hanzo, "Large-scale MIMO is capable of eliminating power-thirsty channel coding for wireless transmission of HEVC/H.265 video," *IEEE Wireless Commun.*, vol. 23, no. 3, pp. 57–63, Jun. 2016.

[15] P. Shen, Y. Qi, W. Yu, J. Fan, Z. Yang, and S. Wu, "A decomposition method for MIMO OTA performance evaluation," *IEEE Trans. Veh. Technol.*, vol. 67, no. 9, pp. 8184–8191, Sep. 2019.

[16] Y. Qi and W. Yu, "Unified antenna temperature," *IEEE Trans. Electromagn. Compat.*, vol. 58, no. 5, pp. 1425–1431, Oct. 2016.

[17] W. Yu, Y. Qi, K. Liu, Y. Xu, and J. Fan, "Radiated two-stage method for LTE MIMO user," *IEEE Trans. Electromagn. Compat.*, vol. 56, no. 6, pp. 1691–1696, Dec. 2014.

[18] Y. Qi *et al.*, "Objective total isotropic sensitivity measurement," *IEEE Trans. Electromagn. Compat.*, vol. 59, no. 6, pp. 1671–1676, Dec. 2017.

[19] A. Alkhateeb, J. Mo, N. Gonzalez-Prelcic, and R. W. Heath, "MIMO precoding and combining solutions for millimeter-wave systems," *IEEE Commun. Mag.*, vol. 52, no. 12, pp. 122–131, Dec. 2014.

[20] W. Fan, P. Kyösti, J. Ø. Nielsen, and G. F. Pedersen, "Wideband MIMO channel capacity analysis in multiprobe anechoic chamber setups," *IEEE Trans. Veh. Technol.*, vol. 65, no. 5, pp. 2861–2871, May 2016.

[21] P. Shen, Y. Qi, W. Yu, and F. Li, "IInverse matrix auto-search technique for the RTS MIMO OTA test—Part 1: Theory," *IEEE Trans. Electromagn. Compat.*, vol. 59, no. 6, pp. 1716–1723, Dec. 2017.

[22] P. Shen, Y. Qi, W. Yu, and F. Li, "Inverse matrix auto-search technique for the RTS MIMO OTA Test—Part II: Validations," *IEEE Trans. Electromagn. Compat.*, vol. 60, no. 5, pp. 1288–1295, Oct. 2018.

[23] C. Schirmer, M. Lorenz, W. A. T. Kotterman, R. Perthold, M. H. Landmann, and G. D. Galdo, "MIMO over-the-air testing for electrically large objects in non-anechoic environments," in *Proc. IEEE 10th Eur. Conf. Antennas Propag.*, Apr. 2016, pp. 1–6.

[24] W. Fan, P. Kyösti, L. Hentilä, and G. F. Pedersen, "MIMO terminal performance evaluation with a novel wireless cable method," *IEEE Trans. Antennas Propag.*, vol. 65, no. 9, pp. 4803–4814, Sep. 2017.

[25] "Radio frequency (RF) requirement background for active antenna system (AAS) base station (BS) radiated requirements," 3GPP, ETSI, Sophia Antipolis, France, Tech. Rep. TR 37.843, 2017.

[26] *Simplified Sectorized MPAC for RRM/Demodulation Setup*, document R4-1705838, Keysight, 3GPP RAN4 Meeting 83, Hangzhou, China, May 2017.
[27] *Active Antenna System (AAS) Base Station (BS) Conformance Testing; Part 2: Radiated Conformance Testing*, document TR 37.145-2, 3GPP, ETSI, Sophia Antipolis, France, 2017.
[28] Q. Huang, F. Zhang, T. Enomoto, J. Maeshima, K. Araki, and C. Hwang, "Physics-based dipole moment source reconstruction for RFI on a practical cellphone," *IEEE Trans. Electromag. Compat.*, vol. 59, no. 6, pp. 1693–1700, Dec. 2017.
[29] Q. Huang *et al.*, "MoM-based ground current reconstruction in RFI application," *IEEE Trans. Electromag. Compat.*, vol. 60, no. 4, pp. 1121–1128, Aug. 2018.
[30] Z. Yan, J. Wang, W. Zhang, Y. Wang, and J. Fan, "A miniature ultrawideband electric field probe based on coax-thru-hole via array for near-field measurement," *IEEE Trans. Instrum. Meas.*, vol. 66, no. 10, pp. 2762–2770, Oct. 2017.
[31] S. Pan and J. Fan, "An efficient method to extract surface-wave poles of green's functions near branch cut in lossy layered media," *IEEE Trans. Antennas Propag.*, vol. 63, no. 1, pp. 439–442, Jan. 2015.
[32] M.-T. Dao, V.-A. Nguyen, Y.-T. Im, S.-O. Park, and G. Yoon, "3D polarized channel modeling and performance comparison of MIMO antenna configurations with different polarizations," *IEEE Trans. Antennas Propag.*, vol. 59, no. 7, pp. 2672–2682, Jul. 2011.
[33] *Spatial Channel Model for Multiple Input Multiple Output (MIMO) Simulations*, document TR 25.996 V13.0.0, Dec. 2015.
[34] P. Wilson, "On correlating TEM cell and OATS emission measurements," *IEEE Trans. Electromagn. Compat.*, vol. 37, no. 1, pp. 1–16, Feb. 1995.
[35] C. A. Balanis, *Antenna Theory: Analysis and Design*, 3rd ed. Hoboken, NJ, USA: Wiley, 2005.
[36] *General Test Systems Inc*. [Online]. Available: http://www.trilsolutions.com/english.php/rayzone
[37] *CTIA & CCSA Combined Comparison Test Plan and Proposal*, Standard MOSG170406, Huawei, Sporton, SGS, HWA-TECH, China Mobile, China Unicom, Balun, Apr. 2017.

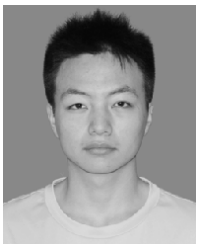

Penghui Shen (S'15) received the B.S. and M.S. degrees in electronic information and technology from Hunan University, Changsha, China, in 2013 and 2016, respectively, where he is currently pursuing the Ph.D. degree in electronics.

His current research interests include SISO, multiple-input multiple output, and 5G array measurements for wireless devices, EMC, and antenna design.

Yihong Qi (M'92–SM'11) received the B.S. degree in electronics from the National University of Defense Technologies, Changsha, China, in 1982, the M.S. degree in electronics from the Chinese Academy of Space Technology, Beijing, China, in 1985, and the Ph.D. degree in electronics from Xidian University, Xi'an, China, in 1989.

From 1989 to 1993, he was a Post-Doctoral Fellow and then an Associate Professor with Southeast University, Nanjing, China. From 1993 to 1995, he was a Post-Doctoral Researcher with McMaster University, Hamilton, ON, Canada. From 1995 to 2010, he was with Research in Motion (Blackberry), Waterloo, ON, Canada, where he was the Director of Advanced Electromagnetic Research. He founded DBJay in 2011, and he is the CTO of ENICE. He is currently the President and the Chief Scientist with General Test Systems, Inc., Shenzhen, China. He is also an Adjunct Professor with the EMC Laboratory, Missouri University of Science and Technology, Rolla, MO, USA, and an Adjunct professor with Hunan University, Changsha. He is an inventor of over 270 published and pending patents.

Dr. Qi has been a Fellow of the Canadian Academy of Engineering since 2018. He was the recipient of the IEEE EMC Society Technical Achievement Award in 2017. He was a Distinguished Lecturer of the IEEE EMC Society for 2014 and 2015 and serves as the Chairman of the IEEE EMC TC-12.

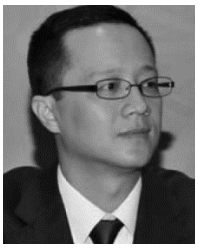

Wei Yu (M'13) received the B.S. degree in electrical engineering from Xi'an Jiaotong University, Xi'an, China, in 1991, the M.S. degree in electrical engineering from the China Academy of Space Technology, Beijing, China, in 1994, and the Ph.D. degree in electrical engineering from Xidian University, Xi'an, China, in 2000.

From 2001 to 2003, he was a Post-Doctoral Fellow with the University of Waterloo, Waterloo, ON, Canada. He was a CTO with Sunway Communications Ltd., from 2008 to 2012. He founded Antenovation Electronics Inc., in 2004 and co-founded General Test Systems Inc., Shenzhen, China, in 2012. He is currently a COO with DBJ Technologies. He is an inventor of 91 published and pending patents. His current research interests include signal processing and mobile device test system.

James L. Drewniak (S'85–M'90–SM'01–F'06) received the B.S., M.S., and Ph.D. degrees in electrical engineering from the University of Illinois at Urbana–Champaign, Urbana, IL, USA, in 1985, 1987, and 1991, respectively.

He is with the Electromagnetic Compatibility Laboratory, Department of Electrical and Computer Engineering, Missouri University of Science and Technology, Rolla, MO, USA. His current research interests include electromagnetic compatibility, signal and power integrity, and electronic packaging.

Ming Yu (S'90–M'93–SM'01–F'09) received the Ph.D. degree in electrical engineering from the University of Victoria, Victoria, BC, Canada, in 1995.

In 1993, he joined COM DEV, Cambridge, ON, Canada, as a Technical Staff Member. He was involved in designing passive microwave/RF hardware for both space and ground-based applications. He was a Principal Developer of a variety of COM DEV's core design and tuning software for microwave filters and multiplexers, including computer-aided tuning software in 1994 and a fully automated robotic diplexer tuning system in 1999. He was a Manager of Filter/Multiplexer Technology (Space Group) and a Staff Scientist of Corporate Research and Development. In 2003, he demonstrated the world's first robotic filter/diplexer tuning system at the IEEE MTT-S IMS conference workshop. Until 2016, he was the Chief Scientist and the Director of Research and Development. He was responsible for overseeing the development of the company's research and development roadmap and next-generation products and technologies, including high-frequency and high-power engineering, electromagnetic-based CAD and tuning for complex and large problems, and novel miniaturization techniques for microwave networks. After COM DEV was acquired by Honeywell in 2016, he has led the Advanced Technology Group, Cambridge, ON, Canada, as the Chief Scientist and a Senior Engineering Fellow. He has been an Adjunct Professor with the University of Waterloo (UW), Waterloo, ON, Canada. After 24 years in industry full time and 15 years as an Adjunct Professor with UW, he joined the Electronics Engineering Department, Chinese University of Hong Kong, as a tenured Full Professor in 2017. He has authored or coauthored over 140 publications and 30 patents worldwide. He served as keynote or invited speakers and session chairs in many international conferences and workshops.

Dr. Yu is a Fellow of the Canadian Academy of Engineering. He holds the NSERC Discovery Grant (2004–2021) with UW and GRF grant with CUHK. He was a recipient of the 1995 and 2006 COM DEV Achievement Award for the development of computer-aided tuning algorithms and systems for microwave filters and multiplexers. He was an IEEE Distinguished Microwave Lecturer from 2010 to 2012. He served as the IEEE MTT-S Filter Committee Chair (MTT-8) and also the Chair of TPC-11 multiple times. He was an Associate Editor of the IEEE TRANSACTIONS ON MICROWAVE THEORY AND TECHNIQUES.

Fuhai Li (M'16) received the B.S. and M.S. degrees in instrument science and technology from Hunan University, Changsha, China, in 1982 and 1988, respectively.

He was a Professor with Hunan University, Changsha, China. He has authored over 22 papers in the national core journals and involved the compiling of university teaching materials.

Mr. Li was a recipient of several science and technology progress awards during his tenure. His students have been the recipients of numerous awards in various national competitions under his leadership.